

Photocatalytic O₂ activation carried out by organic aerosol: A case study of 1, 8-naphthalic anhydride

Tingting Dong^a, Guohui Dong^{a,*}, Yuxin Li^a, Zizhong Zhang^b

^a School of Environmental Science and Engineering, Shaanxi University of Science and Technology, Xi'an 710021, PR China

^b State Key Laboratory of Photocatalysis on Energy and Environment, Fuzhou University, Fuzhou 350116, PR China

ARTICLE INFO

Keywords:

1, 8-naphthalene anhydride
Reactive oxygen species
Built-in electric field , internal polar molecule
Organic aerosol

ABSTRACT

1,8-naphthalene anhydride (1,8-NA) is a common polycyclic aromatic hydrocarbons (PAHs) which are the most important light absorbed-organic aerosols (BrC) in atmospheric. 1,8-NA can generate different ROSs (-OH, ·O₂, H₂O₂, ¹O₂) under the visible light irradiation. According to the results of DFT simulation and band structure analysis, 1,8-NA has the semiconductor characteristic, and the electrons of it can be excited from acid anhydride part to naphthalene ring part. Meanwhile, a built-in electric field exists between the acid anhydride and the naphthalene ring because of the molecular polarization of 1,8-NA. This electric field could promote the separation and migration of carriers. Therefore, electrons can easily be transferred to O₂ and produce ROS. The properties and mechanism of photocatalytic O₂ activation by atmospheric aerosol component 1, 8-NA were studied for the first time, which provided good support for further understanding of atmospheric photochemical mechanism.

1. Introduction

Photochemical reaction is an important cause of the atmospheric secondary pollution.^[1,2] This is because the photochemical reaction can produce O₃, NO and other secondary pollution, which could cause acid rain, haze, and photochemical smog.^[3–8] Meanwhile, there are a lot of particles floating in the air.^[9–11] These particles contain many inorganic and organic semiconductors, which will trigger a series of atmospheric photocatalytic reactions under the light irradiation.^[12–14] Atmospheric photocatalytic reactions could induce redox reactions of O₂ and H₂O, thus producing many reactive oxygen species (ROS) such as hydroxyl radical (-OH), superoxide radical (·O₂) and hydrogen peroxide (H₂O₂).^[15–20] These ROS would kill the airborne bacteria and decompose the volatile organic pollutants (VOCs) by oxidation reaction.^[21–23] Therefore, atmospheric photocatalytic reaction has great influence on atmospheric environment. However, there is very little research in this area.

It is generally believed that atmospheric photochemical reaction is a chain reaction triggered by light, and little attention is paid to the role of atmospheric particles. Atmospheric particles have obvious light scattering and light absorption effects.^[24–26] For example, carbon-containing particles can reduce atmospheric visibility and even

affect the energy balance of the troposphere. Wang et al.^[27] showed that brown carbon sensitization increased the nitrite yield of nitrate photolysis. After the light absorption, some particles can be excited and produce photoinduced carriers. In the meantime, O₂ or H₂O molecules may be adsorbed on the surface of these particles. Thus, the photoinduced carriers may transfer to O₂ or H₂O molecules to induce the redox reactions. ROSs produced over particles can effectively remove and degrade pollutants. For example, Gen and colleagues^[28,29] found that oxidizing agents produced over nitrate particle phase could effectively oxidize inorganic/organic air pollution. Lian's group^[30] found that black nitrogen (DBN) released from black carbon (BC) could produce reactive oxygen species (such as 1 O₂, O₂⁻ and ·OH) to degrade bisphenol A. Recently, our research has shown that environmental persistent free radicals (EPFRs) in atmospheric mineral dust contribute to the photocatalytic production of ROS.^[31] Although there are some researches, the essential cause of photocatalytic ROS production over particles is still unclear.

As we know, light absorbed-organic aerosols (BrC) have the properties of light absorbing and light excitation, and polycyclic aromatic hydrocarbons (PAHs) and their derivatives are the most important BrC chromophores in atmospheric aerosols.^[10,25,32–35] However, the ability of PAHs to act as photocatalysts stably and efficiently has not

* Corresponding author.

E-mail address: dongguohui@sust.edu.cn (G. Dong).



been fully studied. We believe that the studying from this perspective may shed light on why some particles trigger the photocatalytic reactions. As an important atmospheric PAHs, 1,8-naphthalic anhydride (1,8-NA) has been reported to have good light absorption properties (between 300 and 400 nm) and a non-centrosymmetric (NCS) crystal structure.^[36] Thomas et al. used density functional theory and time-varying DFT calculations to understand the electronic structure and absorption properties of 1, 8-NA and its derivatives, revealing the charge transfer characteristics of their low energy absorption bands.^[37] Li et al. found that the first excited state of a "push-pull" molecule composed of triphenylamine groups and 1,8-naphthalic anhydride rings changes from intramolecular charge transfer state (ICT) to intramolecular electron transfer state (ET) with the increase of the number of electron-donating triphenylamine groups.^[38] In recent years, the research on 1,8-NA in the field of organic semiconductors has mainly focused on the preparation of derivatives with tunable fluorescence properties, thus demonstrating the application of this substance in optoelectronics,^[39] dye-sensitized solar cells,^[40] organic light-emitting diode emission materials,^[41] biological system labeling reagents,^[42] polymerization photoinitiators,^[43] etc. In this study, we focus on the fact that the NCS crystal structure of 1, 8-NA allows the dipoles to produce non-overlapping positive and negative charges, resulting in a built-in electric field.^[44–49] The internal electric field is a key dynamic factor to promote the separation and migration of photogenerated carriers in photocatalysts, which is crucial for charge separation.^[50–52] Therefore, we believe that 1,8-NA may have good photocatalytic properties and may play an important role in the generation of ROS in the atmospheric environment.

In this study, we have conducted an in-depth investigation of the photocatalytic activity of 1,8-NA for the first time. It is found that 1,8-NA can activate O₂ molecules under the visible light irrigation to generate corresponding ROS. Moreover, the photocatalytic O₂ activation property of 1,8-NA is better than that of g-C₃N₄ (A classical organic photocatalyst). This is mainly due to the fact that 1,8-NA can be excited by the visible light to produce charge carriers, and its own built-in electric field could help the carrier conduction. The mechanism has been demonstrated in detail.

2. Experimental

2.1. Experimental materials

1,8-naphthalic anhydride (1,8-NA): 1,8-NA was purchased from Shanghai McLean Biochemical Technology Co., Ltd. Melamine was purchased from Sinopharm Chemical Reagent Co., Ltd. All chemicals were analytical grade and used without further purification.

Graphite carbon nitride (CN) sample was prepared using a calcination method. First, 4 g of melamine was placed in a 30 mL crucible, which was then covered with a lid and placed in a muffle furnace. This muffle furnace was heated to 350 °C at a heating rate of 9.5 °C/min and kept for 1 h. Then, the temperature of this muffle furnace was further increased to 520 °C and was kept for 4 h. After the muffle furnace was cooled to the room temperature, the yellow solid in the crucible is graphite carbon nitride, which was ground into the powder and was denoted as CN.

2.2. Characterization

To identify the crystalline phase of the samples, X-ray diffraction (XRD) was performed by the X-ray diffractometer (Bruker D8 Advance) with a monochromated CuKa radiation ($\lambda = 1.5418 \text{ \AA}$). The light absorption abilities of the samples were analyzed by a Shimadzu UV2600 spectrophotometer (Spectral pure BaSO₄ was used as the reference.). Photoluminescence (PL) spectra was measured by an Edinburgh Analytical Instrument FS5 spectrophotometer. Kelvin Probe Force Microscopy (KPFM) tested the surface potential of samples. The test

instrument is a Bruker Dimension Icon. Ultraviolet photo-electron spectroscopy (UPS) was tested at Thermo Scientific ESCALAB Xi+, USA - Thermo Fisher Scientific.

2.3. The detection of H₂O₂ and ·OH through fluorescence probe technique

Fluorescence probe technique is generally used to detect the generated H₂O₂ and ·OH. To prepare the fluorescent reagents, 10 mg of horseradish peroxidase (POD) and 27 mg of p-hydroxy phenylacetic acid (POHP) were added into 100 mL of 8.2 g/L potassium hydrogen phthalate (KHP) solution. Then, above solution was shaken until POD and KHP dissolved. Finally, the generated fluorescent reagent was stored in the refrigerator for the further using.

To detect H₂O₂, 50 mg of the sample powder was added in a glass beaker with 50 mL deionized water. This glass beaker was placed in an ice water bath. Then, the suspension was irradiated with visible light under the continuous stirring. During irradiation, 3 mL of the suspension was taken out from the beaker every 10 minutes and filtered through a 0.22 μm filter. Subsequently, 50 μL of fluorescent reagent was added to react with the generated H₂O₂. After 10 min, 1 mL of NaOH solution was added to terminate the reaction. Finally, the generated H₂O₂ was measured by the fluorescence spectrophotometer (emission at 409 nm, excitation at 315 nm).

Terephthalic (PTA) acid solution was used to detect the ·OH. To prepare the PTA solution, 0.83 g of PTA and 0.4 g of NaOH were added into a 1000 mL glass beaker. Then, 1000 mL of deionized water was added and heated (50 °C) in a water bath equipment with the magnetic stirring for 24 h to dissolve PTA and NaOH. To detect the generated ·OH, 50 mg sample was dispersed into 50 mL of PTA solution under the magnetic stirring. Subsequently, the suspension was irradiated with visible light under the continuous stirring. During irradiation, 4 mL of the suspension was taken out from the beaker every 10 minutes and filtered through a 0.22 μm filter. The filtered liquid was subjected to the fluorescence test (emission at 426 nm and excitation at 312 nm).

2.4. The detection of reactive oxygen species through ESR

A Bruker EMX PLUS instrument was used for the electron spin-resonance (ESR) spectroscopy experiments. 5,5-Dimethyl-L-pyrroline N-oxide (DMPO) was used as the trapping reagent for ·O₂[·] and ·OH. 2,2,6,6-Tetramethylpiperidine (TEMP) was used as the trapping reagent for ¹O₂. 5 mg of samples were mixed in the 40 mM of reagent solution (Methanol dispersion for the ·O₂[·] detection; DI water dispersion for the detection of ·OH and ¹O₂). Then, the suspension was irradiated for 3 min under irradiation ($\lambda > 400 \text{ nm}$), and the supernatant was drawn into a quartz capillary for the ESR measurement. In the detection process, the modulation frequency was 100 kHz; the modulation amplitude was 1 G; the sweep time was 30 s; the field position was 3500 G; the center field was 3510 G; the attenuation was 30 dB.

2.5. Electrochemical analysis

To prepare the working electrodes, 20 mg of samples and 400 μL of absolute ethanol were placed into a 2 mL sample tube which was then suffer from 20 minutes of ultrasonic treatment. Subsequently, this suspension was evenly dripped onto the FTO glass with the size of 2.0 cm × 2.0 cm. Finally, this FTO glass was dried in an oven to obtain the final working electrode.

Photoelectrochemical experiments were performed on an electrochemical workstation (CHI660E) with a three-electrode system. In the testing process, 50 mL of 0.1 mol/L Na₂SO₄ solution was used as the electrolyte. Besides the prepared working electrode, a saturated calomel electrode, a platinum plate (2 cm × 2 cm), and an AgCl electrode were chosen as the reference electrode, the counter electrode, and the reference electrode, respectively. A 300 W Xe lamp with a 400 nm cutoff filter was used as the light source in the detection process. The back surface of

the working electrode was illuminated with the light, which passed through the side face of the three-electrode cell. Electrochemical impedance spectra were obtained by sweeping the frequency from 100 kHz to 0.01 Hz with an AC amplitude method at ambient temperature.

3. Results and discussion

The chemical structure of 1,8-NA can be verified by the FTIR spectroscopy, ^{13}C NMR, and ^1H NMR (Fig. 1). As shown in FTIR spectrum (Fig. 1a), the two bands at 1770 and 1740 cm^{-1} are assigned to the asymmetric stretching and symmetric stretching of the anhydride carbonyl group, respectively; the sharp peak at around 1013 cm^{-1} is attributed to the stretching vibration of C–O–C in the five-membered aromatic anhydride ring; the small peak at about 3067 cm^{-1} originates from the stretching vibration of =CH- in the naphthalene ring unit; the sharp peak at 773 cm^{-1} originates from the out-of-plane bending vibration of C-H. Above FTIR results preliminarily indicate that the sample is 1,8-NA. This result can be further proved by the ^{13}C NMR spectrum and the ^1H NMR spectrum as shown in Fig. 1b and c (The detailed analysis can be found in the Supporting Information).

It is known from the literature that a 1,8-NA unit cell contains four π -conjugated molecular structures (Fig. 1d). [53] The 1,8-NA nanosheets were formed by molecules self-assembled via π - π stacking between the naphthalene plane. The X-ray diffraction (XRD) peaks of the sample is in high accordance with the standard JCPDS card (No. 33-1768) of 1,8-NA (Fig. 1e). Among different peaks, the peak at $2\theta = 11.9^\circ$ can be assigned as π - π stacking, which are the reflections of the two faces (110) and

(040), respectively. Meanwhile, the peak at 23.9° is the reflection of two intersection faces of (021) and (080). The morphology of 1,8-NA nanosheets was analyzed by the transmission electron microscopy (TEM). As shown in Fig. 1f, the morphology of 1,8-NA is a thin ribbon structure with irregular zig-zag edges. This morphology is determined by its crystal structure and the way of π - π stacking. The thickness of 1,8-NA nanosheets is about 1.5 nm, which can be proved by the atomic force microscopy (AFM, Fig. 1g, h). This thickness is exactly equal to the height of 1,8-NA structure cell which is perpendicular to the (040) face. Therefore, 1,8-NA nanoribbons are grown along with the (040) crystal plane through the π stacking. As shown in Fig. 1i, the 1,8-NA nanoribbons exhibit zig-zag edges from the front view. The green plane represents the (040) crystal plane, and the side and top views of the 1,8-NA nanoribbons could be found in Figure S1 and Figure S2. In order to investigate the decomposition temperature of 1,8-NA, thermogravimetric analysis was carried out. As shown in Figs. S3, 1,8-NA starts to decompose at 180°C in the presence of nitrogen atmosphere. Meanwhile, an obvious endothermic peak at 180°C can be seen from the DSC curve. This result shows that 1,8-NA is very stable in the environment. Therefore, it is necessary to study the impact of 1,8-NA on the environment.

It is well known that the redox reactions in the photocatalytic process are mainly performed by the reactive oxygen species (ROSS). [54–56] Therefore, the photocatalytic ROSS generation performance of 1,8-NA was investigated using fluorescent probes and electron spin resonance (ESR) techniques. [57,58] From Figs. 2a and b, 1,8-NA could produce H_2O_2 under visible light irradiation (Fig. 2b shows the reaction process between the H_2O_2 and fluorescent probe). We compared the

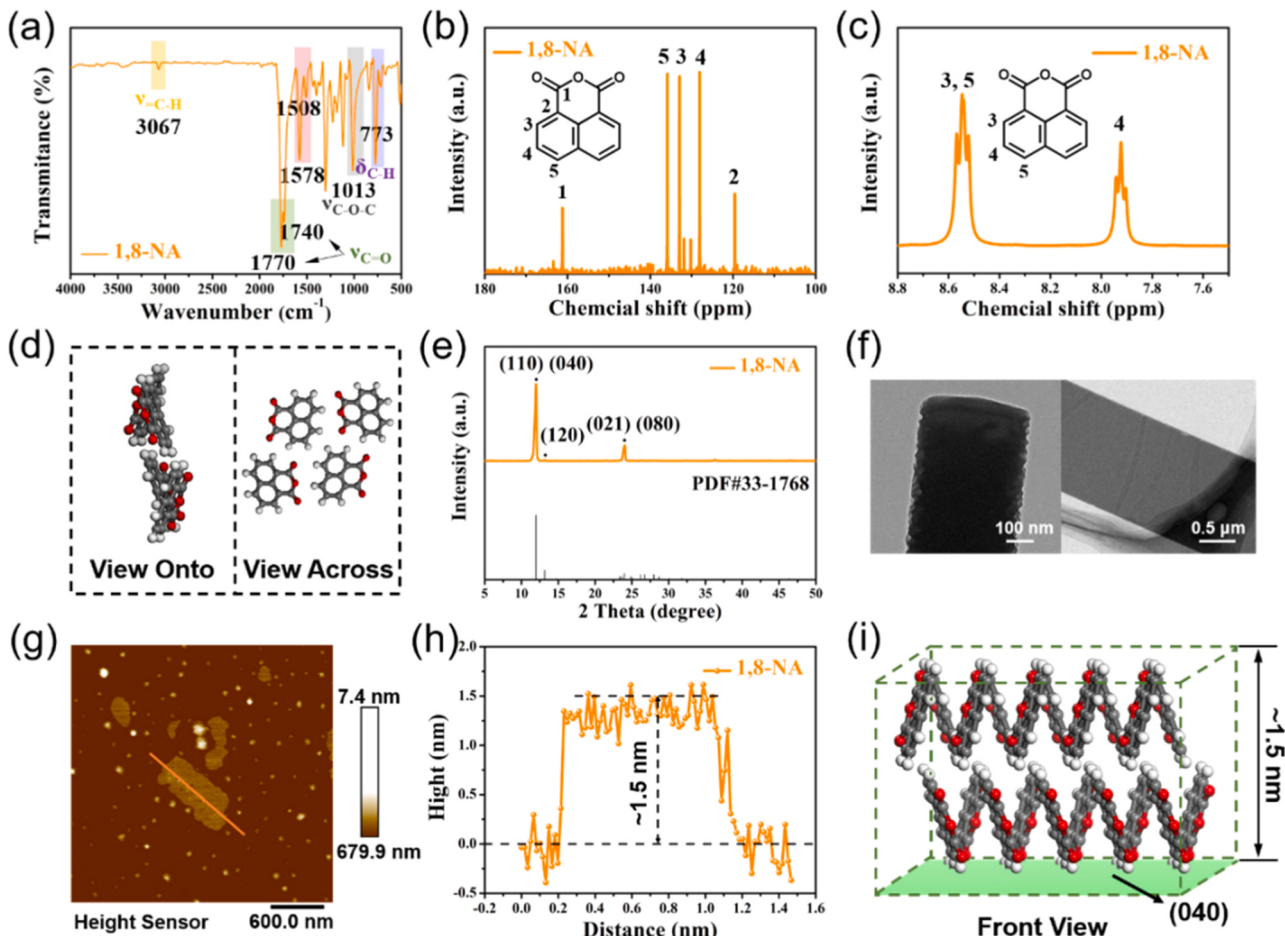


Fig. 1. (a) FT-IR spectrum, (b) ^{13}C NMR spectrum, (c) ^1H NMR spectrum, (d) A cell structure, (e) XRD pattern, (f) TEM images, (g) AFM images, (h) Corresponding thickness curve, and (i) Schematic diagram of the front view after π - π stacking of 1,8-NA sample.

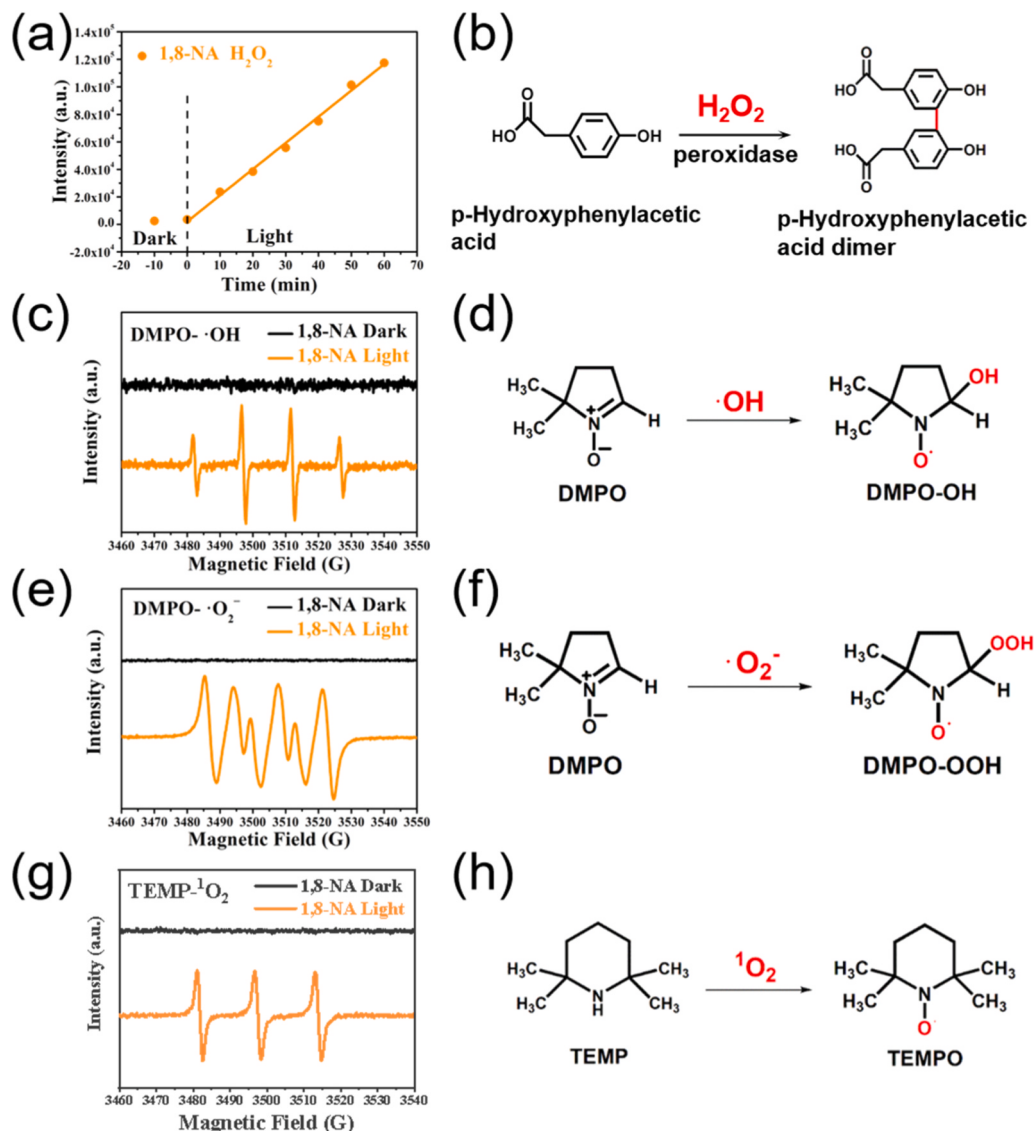


Fig. 2. (a) Generation curve of H_2O_2 on 1,8-NA samples, (b) The reaction process between the H_2O_2 and fluorescent probe, (c) DMPO spin-trapping electron paramagnetic resonance spectra recorded for $\bullet\text{OH}$ in the 1,8-NA systems, (d) Reaction process of DMPO spin-trapping $\bullet\text{OH}$, (e) DMPO spin-trapping electron paramagnetic resonance spectra recorded for $\bullet\text{O}_2^-$ in the 1,8-NA systems, (f) Reaction process of DMPO spin-trapping $\bullet\text{O}_2^-$, (g) TEMP spin-trapping electron paramagnetic resonance spectra recorded for $^1\text{O}_2$ in the 1,8-NA systems, and (h) Reaction process of TEMP spin-trapping $^1\text{O}_2$.

photocatalytic H_2O_2 production performance of 1,8-NA with that of g-C₃N₄ (Labeled as CN) because CN is a classic organic photocatalytic material. It can be found that the H_2O_2 yield of 1,8-NA is about twice that of CN under the same condition (Figure S4 and S5). For ESR is a classic method to detect free radicals, the generated $\bullet\text{OH}$ in 1,8-NA systems can be proved by the ESR detection as shown in Fig. 2c. 1,8-NA has no signal in the dark condition. After 3 min of light irradiation, a quadruple ESR signal with the peak ratio of 1:2:2:1 can be detected. This ESR signal can be attributed to the $\bullet\text{OH}$ signal. Fig. 2d shows the reaction mechanism of 5,5-dimethyl-1-pyrroline N-oxide (DMPO) and $\bullet\text{OH}$. After the fluorescent probe experiment, it can be found that the $\bullet\text{OH}$ generated by 1,8-NA is 1.6 times more than that generated by CN (Figure S6). Through the ESR test, it can also be found that 1,8-NA can generate $\bullet\text{O}_2^-$ and $^1\text{O}_2$ under the visible light irradiation (Fig. 2e, f, g, h). Their intensity contrast is shown in the Supporting Information (Figure S7). Above experiments demonstrate that 1,8-NA can generate different ROSS under the visible light irradiation.

To investigate the reason why 1,8-NA sample has photocatalytic performances, the frontier molecular orbital distribution of 1,8-NA

molecule has been analyzed based on the DFT simulation. As shown in Fig. 3, in the excited state, the occupied orbitals of HOMO-2 are mainly distributed in the acid anhydride part, and the unoccupied orbitals of LUMO+2 are mainly distributed in the naphthalene ring part. This phenomenon suggests that 1,8-NA has the semiconductor characteristic, and the electrons of it can be excited from acid anhydride part to naphthalene ring part.

The band structure of 1,8-NA was also investigated. Firstly, the light absorption ability of the 1,8-NA sample was investigated via UV-vis absorption spectrum. As shown in Figs. 3b, 1,8-NA shows a UV-vis absorption spectrum of typical semiconductor. The UV-vis absorption edge of 1,8-NA is at 400 nm, which is smaller than that of CN. According to the Kubelka-Munk function, the band gap of 1,8-NA is calculated to be 3.06 eV, which is larger than that of CN (2.8 eV, Fig. 3c). Density of States (DOS) was also simulated to determine the band gap of the 1,8-NA. The band gap shown on the DOS plot is 2.34 eV (Fig. 3d). Besides the bandgap, the positions of the valence band (E_{VB}) and conduction band (E_{CB}) have great influence on the photocatalytic redox ability.[45, 58] To further clear the band structure of 1,8-NA, ultraviolet

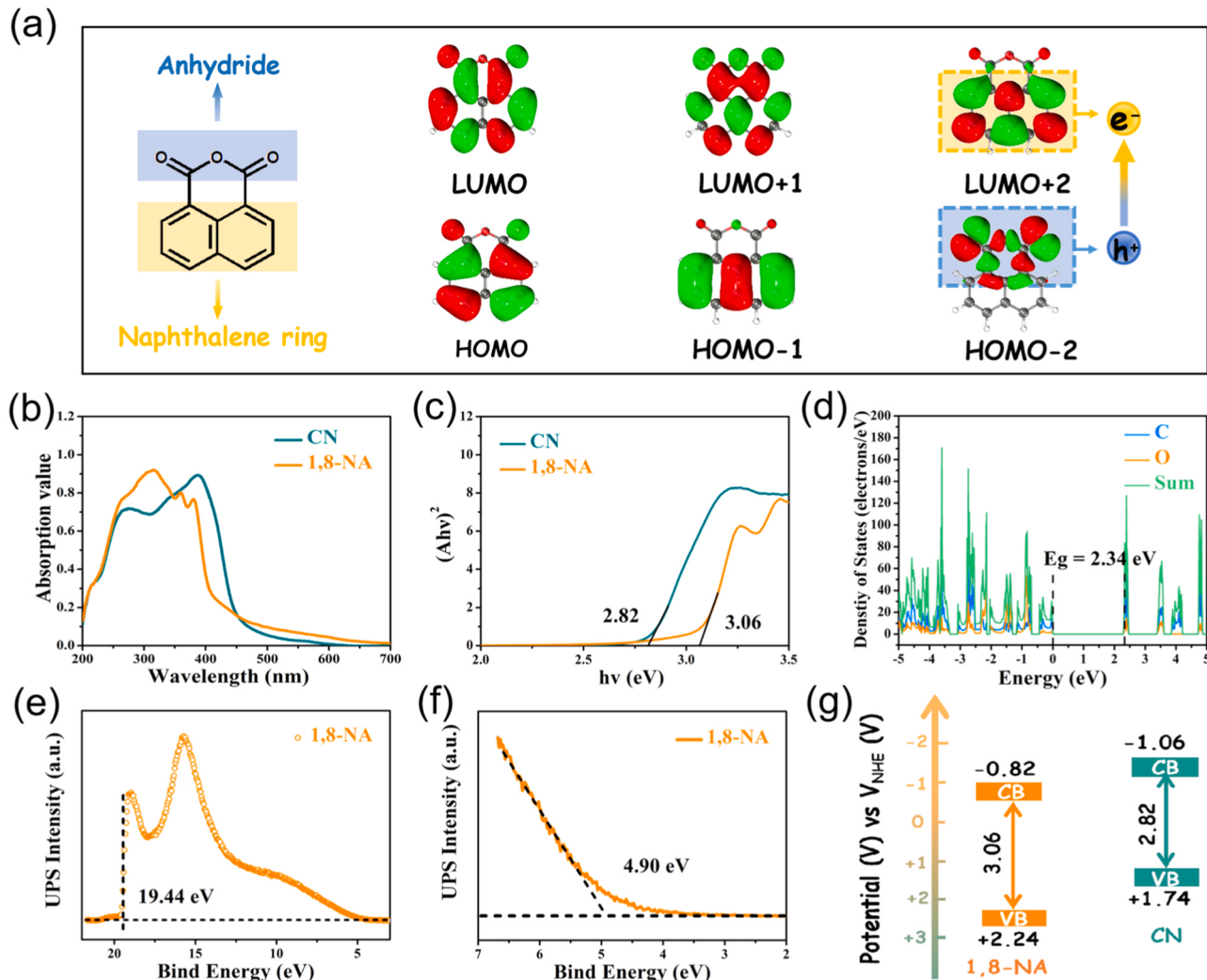


Fig. 3. (a) DFT simulation of molecular orbital distribution at the front of 1,8-NA molecule, (b) UV-vis images and (c) Band gap images of CN and 1,8-NA samples, (d) DOS images, (e) Secondary electron cutoff (E_{cutoff}) of UPS spectra, (f) The lowest kinetic energy onset edge is in the UPS spectrum, and (g) schematic diagram of the positions of the VB and CB of 1,8-NA and CN samples.

photoelectron spectroscopy (UPS) and Mott-Schottky experiments were performed to determine the E_{VB} and E_{CB} of 1,8-NA. From Fig. 3e, f, and Table S1, the E_{VB} value of 1,8-NA was calculated to be 2.24 eV vs. NHE (Detailed analysis can be found in the Supporting Information). According to the Mott-Schottky plot, the positive slope suggests that 1,8-NA is an n-type semiconductor (Figure S8). The E_{fb} minimum is estimated to be -0.82 V vs NHE. Since the E_{CB} of n type semiconductor is consistent with the E_{fb} , the E_{CB} value of 1,8-NA is -0.82 V vs NHE. This value is consistent with the calculation result of UPS. Combining with the flat band potential (E_{fb}) results of CN (Figure. S9), the schematic diagram of band positions of 1,8-NA and CN can be obtained (Fig. 3g).

The generation of photogenerated carriers is one of the important signs of photocatalysts. According to the size of the band gap, it was concluded that 1,8-NA nanosheets could be excited by wavelengths below 405 nm. A series of characterizations such as fluorescence spectra of the samples were carried out. To detect the fluorescence spectra of 1,8-NA and CN, these two samples were excited by the light at a wavelength of 370 nm. [59–62] From Fig. 4a, the CN emission peak is at 460 nm, and the 1,8-NA emission peak is at 440 nm, which is consistent with their absorption spectra. To analyze the electron migration effects of different samples, time-resolved PL decay spectra (TRPL), photocurrent density curves, and electrical impedance spectroscopy (EIS) of different samples were detected. [60] Fig. 4b shows the TRPL curves of

different samples under excitation at 325 nm. Obviously, the excited state of 1,8-NA has a longer lifetime than that of CN (specific analysis in Supporting Information). [63] Meanwhile, the photocurrent intensity of 1,8-NA is 1.5 times that of CN, and the impedance of 1,8-NA is significantly less than the impedance of CN (Fig. 4c, d). These phenomena prove that 1,8-NA has better carrier migration effects than CN.

After the generation of photogenerated electrons and holes, the electrons and holes need to be separated to induce the reduction reactions and oxidation reactions. To analyze the separation effect of electrons and holes, Electrostatic potential (ESP) distribution of 1,8-NA was simulated through the computer. The negative region was marked in red and the positive region was marked in blue. From Fig. 5a, it can be found that the darker red area is mainly concentrated in the part of the acid anhydride after applying an electron on the surface of 1,8-NA. Meanwhile, the darker blue region is mainly concentrated in the part of the naphthalene ring after applying a hole on the surface of 1,8-NA (Fig. 5b). These phenomena indicate that there is a polarization field in the 1,8-NA molecule. [45, 46, 64, 65] This can be further clear seen from the ESP distribution of 1,8-NA without applying electron or hole (Fig. 5c). As shown in Fig. 5d, the electrons are mainly concentrated in the part of the acid anhydride, and holes is mainly concentrated in the part of the naphthalene ring. In this case, an electric field can be created between the acid anhydride and the naphthalene ring because of the

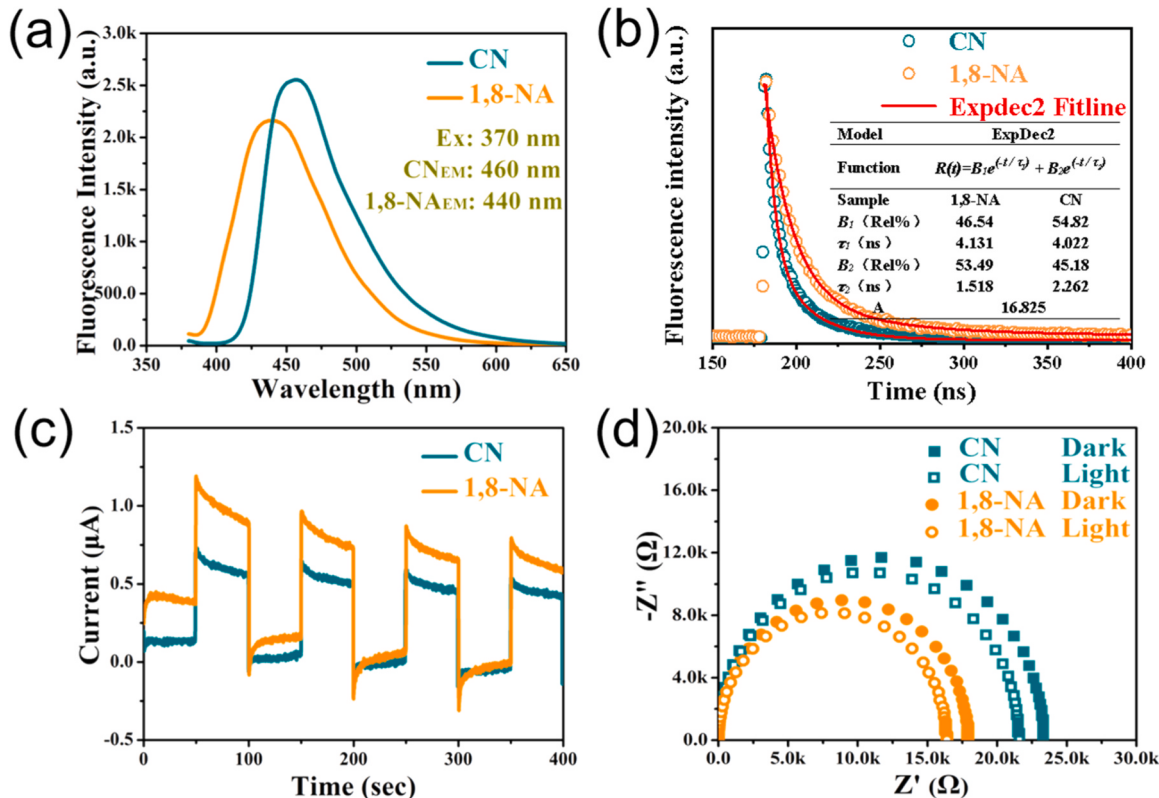


Fig. 4. (a) Fluorescence spectra and (b) TRPL curves of CN and 1,8-NA samples (inset: instrument second order fitting results), (c) Photocurrent densities and (d) EIS spectra of CN and 1,8-NA samples.

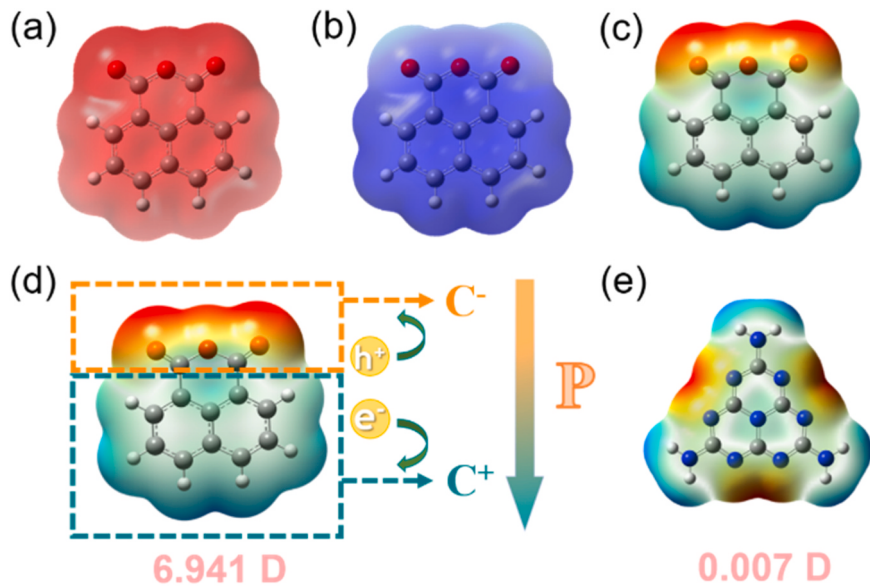


Fig. 5. The EPS of (a) 1,8-NA-anion, (b) 1,8-NA-cation and (c) 1,8-NA. (d) Schematic diagram of polarization mechanism, and (e) The EPS of CN.

molecular polarization of 1,8-NA. This electric field could act as the driving force for the carrier separation and transportation. Compared with the EPS of 1,8-NA, that of CN do not show a clear polarization direction. More importantly, the dipole of 1,8-NA is 6.941 Debye, which is much larger than that of CN (0.007 Debye). Therefore, it can be speculated that 1,8-NA has better carrier separation and migration effects than CN.

The effect of internal electric field is a primary kinetic factor affecting the charge separation. Since internal electric field is positively

correlated with the surface potential, the surface potential can be obtained through the atomic force microscopy with a Kelvin probe (KPFM) as shown in Fig. 6. Fig. 6a and b show the surface potential images of CN and 1,8-NA in the darkness, respectively. The bright areas in the images indicate the higher surface voltage, and the dark areas indicate the lower surface voltage. Obviously, the potential difference on the 1,8-NA surface is significantly higher than that of CN surface. In order to quantitatively determine surface potential differences, the corresponding surface potential difference values for CN and 1,8-NA are analyzed. As

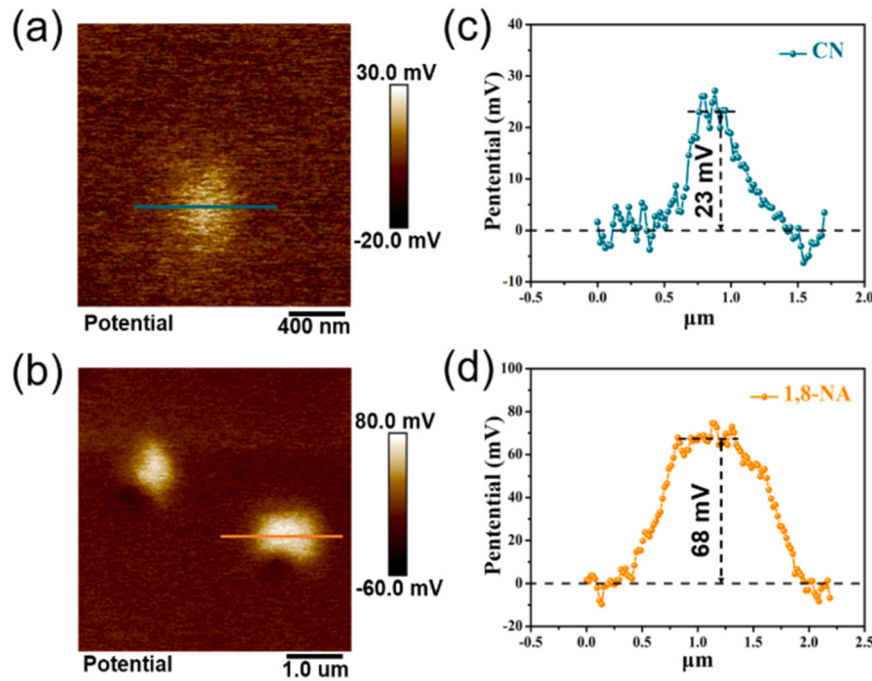


Fig. 6. The KPFM phase images of (a) CN, (b) 1,8-NA. The corresponding surface potential profiles of (c) CN and (d) 1,8-NA.

shown in Fig. 6c, d, the surface potential difference value of 1,8-NA is calculated to be 68 mV, which is much higher than that of CN (23 mV). According to Kanata theory, internal electric fields (IEF) can also be reflected by the product of surface photocharge density and open circuit potential as shown in Figure S10 (specific analysis in S2.5 of Supporting Information). These results strongly demonstrate the highly enhanced

internal electric field existed in the bulk of 1,8-NA compared to CN, which provides a strong driving force for the charge separation of 1,8-NA. Meanwhile, these results are consistent with the analysis results of ESP.

To make the results more convincing, we determined the orientation of IEF by light deposition experiment. Using ammonium oxalate as hole

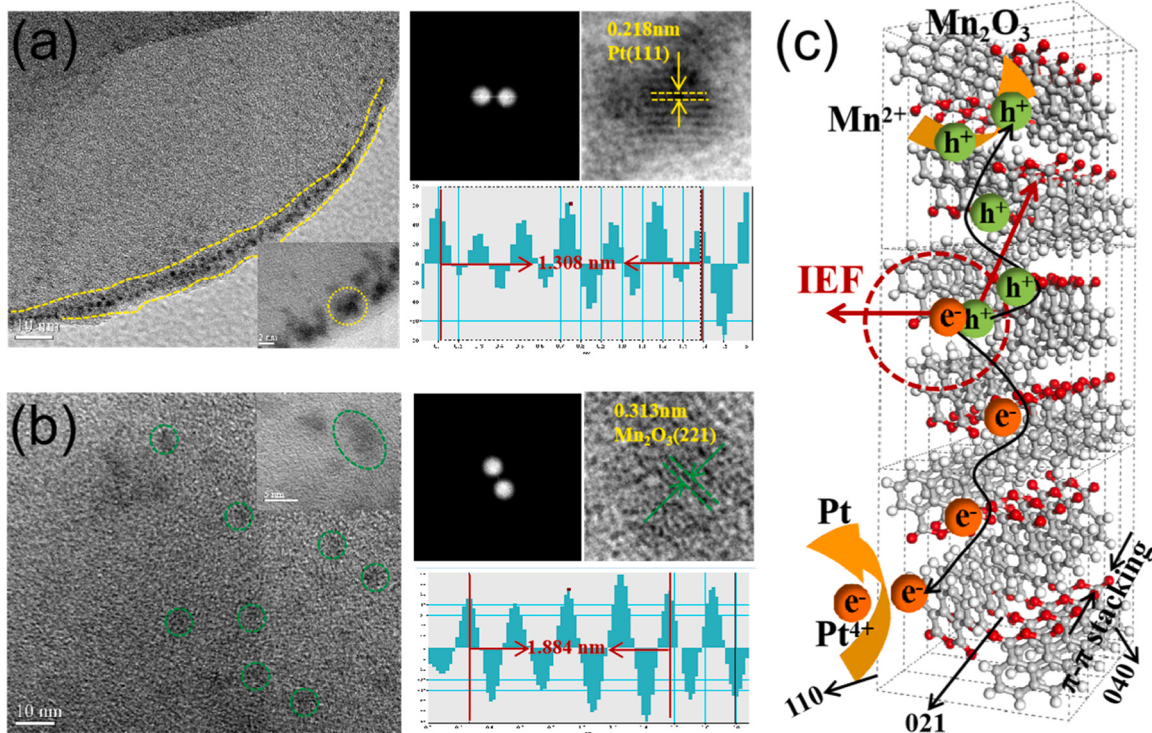


Fig. 7. HRTEM photodeposition on 1,8-NA with a Pt and high resolution (a) and Mn₂O₃ (b). (c) Schematic illustration of Pt and Mn₂O₃ photodeposition on 1,8-NA under visible light ($\lambda \geq 420$ nm). Deposition method: 25 mg of 1,8-NA was dispersed in 25 mL of deionized water, and 4 wt% H₂PtCl₆ (weighed by Pt) or 5 wt% MnCl₂ (weighed by Mn) was added and exposed to visible light ($\lambda \geq 420$ nm) for 3 h.

scavenger, metal ions (Pt^{4+}) are reduced to Pt by photogenerated electrons. HRTEM images (Fig. 7a) clearly show that Pt particles are deposited almost at the edge of 1, 8-NA (i.e., the (110) surface). Therefore, photogenerated electrons tend to migrate to the (110) plane. Using NaIO_3 as electron scavenger, Mn^{2+} can be oxidized to Mn_2O_3 by photogenerated holes. HRTEM images (Fig. 7b and S11) clearly show that Mn_2O_3 particles are deposited almost at the plane of 1, 8-NA (i.e., the (021) surface). Thus, photogenerated holes tend to migrate to the (021) plane. Based on above results, the orientation of IEF can be analyzed from the deposition sites of Mn_2O_3 and Pt. The model shown in Fig. 7c describes the IEF-driven photogenerated carrier migration.

As we all know, the production of ROSs is inseparable from the participation of O_2 . Therefore, it is meaningful to study the O_2 adsorption on the surface of 1,8-NA. According to the electron arrangement in the outer shell of O_2 , each oxygen atom of O_2 has a single electron (Fig. 8a). Since the C atoms of 1,8-NA are Sp^2 hybridized, there will be a single electron on each C atom. In this way, the O atom of O_2 may form a covalent bond with the C atom. Therefore, we analyze that O_2 may be adsorbed on the naphthalene ring part. To further illustrate the adsorption sites of oxygen, we calculated the adsorption sites and adsorption energies of O_2 on the surface of 1,8-NA by DFT theoretical simulation. As shown in Fig. 8b, the structure of the O_2 molecule and the naphthalene anhydride molecule was optimized to make it in a stable structure. Secondly, after computer theoretical simulation, four different adsorption sites 1 ~ 4 can be obtained for reference, corresponding adsorption energies are -1.36 , -2.17 , -0.14 , and -0.15 eV, respectively (Fig. 8c). According to this result, all of these four adsorption sites can occur spontaneously. Additionally, these four adsorption sites are located on the naphthalene ring. From the ESP analysis results, it can be seen that electrons are transferred to the naphthalene ring. Therefore, the O_2 adsorption sites are consistent with the O_2 reduction process.

To further elucidate the H_2O_2 production mechanism of 1,8-NA, a series of active species trapping experiments were carried out. Fig. 9a shows the photocatalytic H_2O_2 production in the presence of the electron scavenger and the hole scavenger. It can be found that the H_2O_2 generation is greatly attenuated after the addition of the electron

scavenger (AgNO_3) and the hole scavenger ($(\text{NH}_4)_2\text{C}_2\text{O}_4$), suggesting H_2O_2 production process may be a tandem reaction between photo-generated holes and photogenerated electrons. During this tandem reaction, other ROSs (Such as $\cdot\text{O}_2$, 1O_2 , $\cdot\text{OH}$) may be involved. Therefore, ROSs' capture experiments were also conducted. From Fig. 9b, both the capture of $\cdot\text{O}_2^-$ and 1O_2 significantly inhibit the generation of H_2O_2 . $\cdot\text{O}_2^-$ and 1O_2 may act as the intermediates of the generated H_2O_2 . Figure S12 shows that the capture of $\cdot\text{OH}$ could improve the yield of H_2O_2 , indicating $\cdot\text{OH}$ does not contribute to the generation of H_2O_2 . The enhanced H_2O_2 production mainly attributes to the H^+ which from the oxidation reaction of IPA. This is because the generation of H_2O_2 needs the participation of H^+ . The production of H_2O_2 by 1,8-NA at different pH also further supports this explanation (Figure S13, specific analysis in Supporting Information).

To further clear the pathway of H_2O_2 production, the production processes of $\cdot\text{O}_2^-$ and 1O_2 were studied. As shown in Fig. 9c, the electron capture could suppress the generation of $\cdot\text{O}_2^-$, suggesting $\cdot\text{O}_2^-$ is generated from the reduction reaction of O_2 (Eq. 1). Generally, 1O_2 can be produced through two possible paths. One is energy transfer mechanism, and the other is hole oxidation reaction of $\cdot\text{O}_2^-$ (Eq. 2). From Fig. 9d, the 1O_2 signal decreased sharply after adding electron scavenger (AgNO_3) or the hole scavenger ($(\text{NH}_4)_2\text{C}_2\text{O}_4$). This result indicates that the generation of 1O_2 in our system is due to the second path. Therefore, the generation of 1O_2 in our system needs two steps: (1) O_2 is reduced to $\cdot\text{O}_2^-$ by electrons (Eq. 1); (2) the generated $\cdot\text{O}_2^-$ is oxidized to 1O_2 by hole (Eq. 2). Previous literatures have demonstrated that 1O_2 can be reduced to H_2O_2 by electrons. [66–71] As shown in Figure S14, the 1O_2 signal drops sharply after the addition of $\cdot\text{O}_2^-$ scavenger PBQ, which indicates that 1O_2 in the system is produced by $\cdot\text{O}_2^-$ oxidation. Therefore, the path of the tandem reaction is $\text{O}_2 \rightarrow \cdot\text{O}_2^- \rightarrow 1\text{O}_2 \rightarrow \text{H}_2\text{O}_2$ (Eqs. 1, 2 and 3).

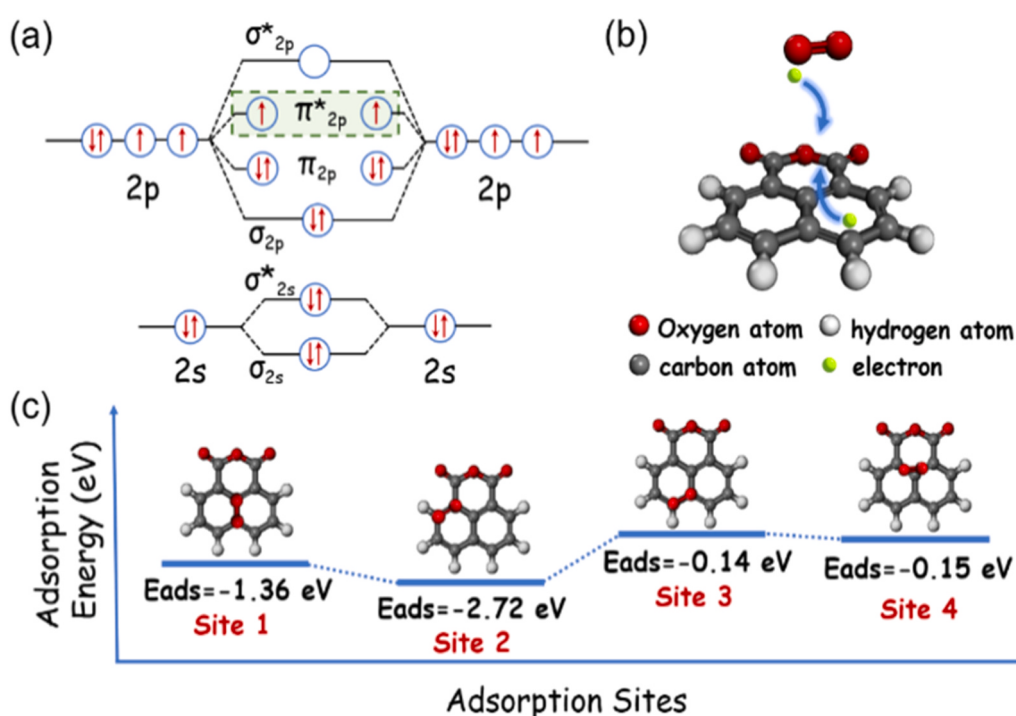


Fig. 8. (a) Oxygen molecule orbital energy level diagram, (b) Schematic diagram of oxygen adsorption by 1,8-NA, and (c) Oxygen adsorption sites and adsorption energy obtained from theoretical simulations.

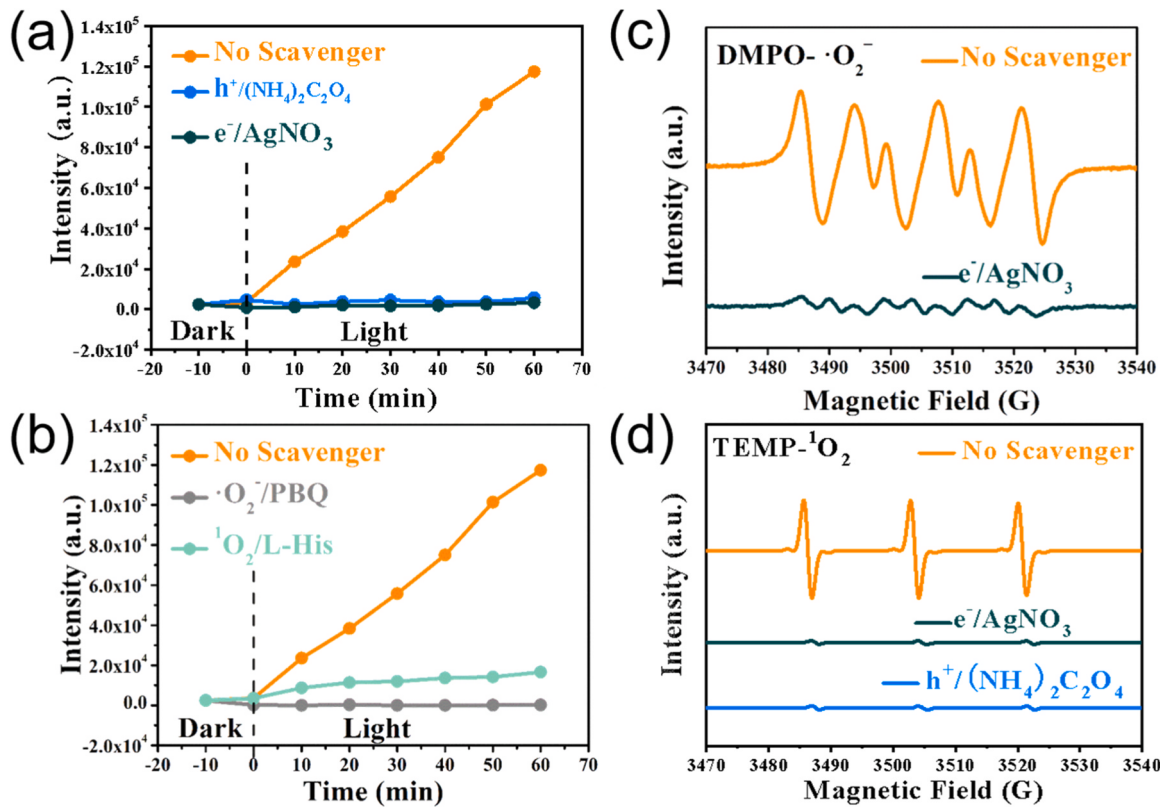


Fig. 9. (a-b) The influence of scavengers on the photocatalytic H_2O_2 production using 1,8-NA (The photocatalysis conditions are the same as in Fig. 2a), (c) DMPO spin trapping ESR technique to measure $\cdot\text{O}_2^-$ generated photoreaction with the addition of AgNO_3 over 1,8-NA, and (d) TEMP spin trapping ESR technique to measure ${}^1\text{O}_2$ generated photoreaction with the addition of AgNO_3 and $(\text{NH}_4)_2\text{C}_2\text{O}_4$ over 1,8-NA.



According to these equations, three electrons and one hole are involved in this tandem reaction process. In the photocatalytic reaction process, one hole could be produced when an electron is generated, meaning that there will be two more holes in the tandem reaction process. What are these two extra holes doing in the H_2O_2 producing process? In the previous mechanism analysis, it can be found that $\cdot\text{OH}$ did not participate in the H_2O_2 production. Therefore, we believe that the extra holes oxidize the OH^- to $\cdot\text{OH}$ (Eq. 4). This conclusion can be

further proved by ESR capture experiments (Figure S15).

In order to investigate the stability of 1,8-NA, the reaction time was extended to 240 minutes. As shown in Figs. S16, CN and 1,8-NA can stably and continuously produce H_2O_2 under the visible light irradiation. However, the H_2O_2 production rate and yield of 1,8-NA are significantly higher than those of CN. To investigate the decomposition behavior of H_2O_2 over different catalysts, the photocatalytic H_2O_2 decomposition over different catalysts has been conducted with an initial H_2O_2 concentration of 1 mM. As shown in Figure S17, H_2O_2 hardly decomposes on the surface of 1,8-NA and CN. To further check the stability of 1,8-NA during the generation of ROSS, the recycling

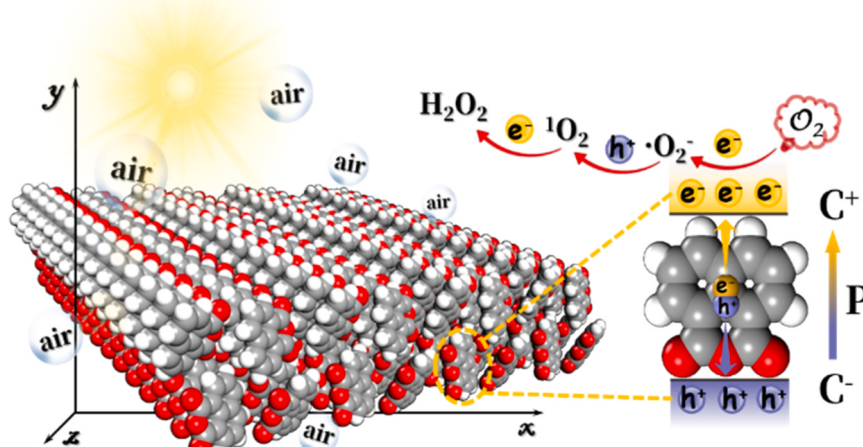


Fig. 10. Schematic representation of H_2O_2 formation on 1,8-NA nanosheet.

experiments were explored. As shown in Figure S18 and S19, the photocatalytic H₂O₂ (•OH) production activity of 1,8-NA did not decrease significantly after 5 cycles. Meanwhile, the FT-IR and XRD patterns of 1,8-NA (Figure S20 and S21) after the reaction are the same as those before the recycling experiments. Based on the above studies, it is indicated that 1,8-NA nanosheets have stable photocatalytic performance, and the schematic diagram of the photocatalytic mechanism is shown in Fig. 10. Besides the O₂ activation, we explored the applications of 1,8-NA in bactericidal and organic pollutant degradation. Under the visible light irradiation, 1,8-NA has a good bactericidal effect on *E. coli* (Figure S22). In addition, 1,8-NA can effectively degrade tetracycline in water. After 1 hour of visible light irradiation, the removal rate of tetracycline can reach 46% (Figure S23). All these performances are due to the fact that 1,8-NA can produce strong reactive oxygen species, which can act on bacteria and organic matter. In the future, the properties and mechanism of 1,8-NA in bactericidal and organic pollutant degradation will be studied in detail.

4. Conclusion

1,8-NA is a common polycyclic aromatic hydrocarbons (PAHs), which are the most important light absorbed-organic aerosols (BrC) in atmospheric. The morphology of 1,8-NA is a thin ribbon structure with irregular zig-zag edges. According to the results of DFT simulation and band structure analysis, 1,8-NA has the semiconductor characteristic. Therefore, the electrons of 1,8-NA can be excited from acid anhydride part to naphthalene ring part. At the same time, there are 4 chemisorption sites (C) for O₂ on the surface of 1,8-NA, and these sites are the places of electrons accumulation. In this way, 1,8-NA can generate different ROSs (•OH, •O₂, H₂O₂ and ¹O₂) under the visible light irradiation. The photocatalytic ROSs production activity of 1,8-NA is better than that of g-C₃N₄. The reason is that a built-in electric field exists between the acid anhydride and the naphthalene ring, and this electric field could promote the separation and migration of carriers. These sites are just the places of electrons accumulation. As the result, the generated electrons can easily be transferred to O₂ and produce ROS.

Contribution statement

Guohui Dong designed the experiments and analyzed data; **Tingting Dong and Yuxin Li** performed the experiments and prepared the manuscript. **Zizhong Zhang** performed conducted data review and article correction.

CRediT authorship contribution statement

Tingting Dong: Writing – review & editing, Writing – original draft, Software, Investigation, Data curation. **Guohui Dong:** Writing – review & editing, Supervision, Resources. **Yuxin Li:** Writing – original draft, Investigation. **Zizhong Zhang:** Writing – review & editing, Supervision.

Declaration of Competing Interest

The authors declare that they have no known competing financial interests or personal relationships that could have appeared to influence the work reported in this paper.

Data Availability

Data will be made available on request.

Acknowledgements

Financial support by the National Natural Science Foundation of China (Grant No. 21876104, 21603109) is gratefully acknowledged. Supported by the Open Project Program of the State Key Laboratory of

Photocatalysis on Energy and Environment (Grant No. SKLPEE-KF 202312), Fuzhou University.

Supporting Information

Supplementary data associated with this article can be found in the online version.

Appendix A. Supporting information

Supplementary data associated with this article can be found in the online version at doi:10.1016/j.apcatb.2024.123889.

References

- [1] M.O. Andreae, P.J. Crutzen, Atmospheric aerosols: biogeochemical sources and role in atmospheric chemistry, *Science* 276 (1997) 1052–1058, <https://doi.org/10.1126/science.276.5315.1052>.
- [2] F.J. Dentener, G.R. Carmichael, Y. Zhang, J. Lelieveld, P.J. Crutzen, Role of mineral aerosol as a reactive surface in the global troposphere, *J. Geophys. Res. Atmos.* 101 (1996) 22869–22889, <https://doi.org/10.1029/96JD01818>.
- [3] D. Wang, B. Zhou, Q. Fu, Q. Zhao, Q. Zhang, J. Chen, X. Yang, Y. Duan, J. Li, Intense secondary aerosol formation due to strong atmospheric photochemical reactions in summer: observations at a rural site in eastern Yangtze River Delta of China, *Sci. Total Environ.* 571 (2016) 1454–1466, <https://doi.org/10.1016/j.scitotenv.2016.06.212>.
- [4] J. Xu, W. Hu, D. Liang, P. Gao, Photochemical impacts on the toxicity of PM_{2.5}, *Crit. Rev. Env. Sci. Tec.* 52 (2022) 130–156, <https://doi.org/10.1080/10643389.2020.1816126>.
- [5] C.A. Weitekamp, T. Stevens, M.J. Stewart, P. Bhave, M.I. Gilmore, Health effects from freshly emitted versus oxidatively or photochemically aged air pollutants, *Sci. Total Environ.* 704 (2020) 135772, <https://doi.org/10.1016/j.scitotenv.2019.135772>.
- [6] X. Fu, T. Wang, J. Gao, P. Wang, Y. Liu, S. Wang, B. Zhao, L. Xue, Persistent heavy winter nitrate pollution driven by increased photochemical oxidants in northern China, *Environ. Sci. Technol.* 54 (2020) 3881–3889, <https://doi.org/10.1021/acs.est.9b07248>.
- [7] A.C. Lewis, The changing face of urban air pollution, *Science* 359 (2018) 744–745, <https://doi.org/10.1126/science.aar4925>.
- [8] M. Zhou, G. Dong, F. Yu, Y. Huang, The deep oxidation of NO was realized by Sr multi-site doped g-C₃N₄ via photocatalytic method, *Appl. Catal. B: Environ.* 256 (2019) 117825, <https://doi.org/10.1016/j.apcatb.2019.117825>.
- [9] M. Abou-Ghanem, A.O. Oliynyk, Z. Chen, L.C. Matchett, D.T. McGrath, M.J. Katz, A.J. Locock, S.A. Styler, Significant variability in the photocatalytic activity of natural titanium-containing minerals: implications for understanding and predicting atmospheric mineral dust photochemistry, *Environ. Sci. Technol.* 54 (2020) 13509–13516, <https://doi.org/10.1021/acs.est.0c05861>.
- [10] P. Corral Arroyo, G. David, P.A. Alpert, E.A. Parmentier, M. Ammann, R. Signorell, Amplification of light within aerosol particles accelerates in-particle photochemistry, *Science* 376 (2022) 293–296, <https://doi.org/10.1126/science.abm7915>.
- [11] H. Maleki, N. Hüsing, Current status, opportunities and challenges in catalytic and photocatalytic applications of aerogels: environmental protection aspects, *Appl. Catal. B Environ.* 221 (2018) 530–555, <https://doi.org/10.1016/j.apcatb.2017.08.012>.
- [12] J. Ye, Y. Chen, C. Gao, C. Wang, A. Hu, G. Dong, Z. Chen, S. Zhou, Y. Xiong, Sustainable conversion of microplastics to methane with ultrahigh selectivity by a biotic-abiotic hybrid photocatalytic system, *Angew. Chem. Int. Ed.* 61 (2022) e202213244, <https://doi.org/10.1002/anie.202213244>.
- [13] M.A. Kebede, M.E. Varner, N.K. Scharko, R.B. Gerber, J.D. Raff, Photooxidation of ammonia on TiO₂ as a source of NO and NO₂ under atmospheric conditions, *J. Am. Chem. Soc.* 135 (2013) 8606–8615, <https://doi.org/10.1021/ja401846x>.
- [14] X. Xu, K. Xie, J. Hu, S. Liu, H. Zhong, H.-R. Wen, The metal-organic frameworks as unique platform for photocatalytic CO₂ conversion to liquid fuels, *J. Environ. Chem. Eng.* 11 (2023), <https://doi.org/10.1016/j.jece.2023.110424>.
- [15] P. Liu, C. Ye, C. Zhang, G. He, C. Xue, J. Liu, C. Liu, Y. Zhang, Y. Song, X. Li, Photochemical aging of atmospheric fine particles as a potential source for gas-phase hydrogen peroxide, *Environ. Sci. Technol.* 55 (2021) 15063–15071, <https://doi.org/10.1021/acs.est.1c04453>.
- [16] Y. Nosaka, A.Y. Nosaka, Generation and detection of reactive oxygen species in photocatalysis, *Chem. Rev.* 117 (2017) 11302–11336, <https://doi.org/10.1021/acscchemrev.7b00161>.
- [17] H. Wang, S. Jiang, W. Shao, X. Zhang, S. Chen, X. Sun, Q. Zhang, Y. Luo, Y. Xie, Optically switchable photocatalysis in ultrathin black phosphorus nanosheets, *J. Am. Chem. Soc.* 140 (2018) 3474–3480, <https://doi.org/10.1021/jacs.8b00719>.
- [18] X. Sheng, Z. Liu, R. Zeng, L. Chen, X. Feng, L. Jiang, Enhanced photocatalytic reaction at air-liquid-solid joint interfaces, *J. Am. Chem. Soc.* 139 (2017) 12402–12405, <https://doi.org/10.1021/jacs.7b07187>.
- [19] L. Yang, P. Wang, J. Yin, C. Wang, G. Dong, Y. Wang, W. Ho, Engineering of reduced graphene oxide on nanosheet-g-C₃N₄/perylene imide heterojunction for enhanced photocatalytic redox performance, *Appl. Catal. B: Environ.* 250 (2019) 42–51, <https://doi.org/10.1016/j.apcatb.2019.02.076>.

[20] X. Xu, Y. Sui, W. Chen, W. Huang, X. Li, Y. Li, D. Liu, S. Gao, W. Wu, C. Pan, H. Zhong, H.-R. Wen, M. Wen, The photocatalytic H_2O_2 production by metal-free photocatalysts under visible-light irradiation, *Appl. Catal. B Environ.* 341 (2024) 123271, <https://doi.org/10.1016/j.apcatb.2023.123271>.

[21] H.P. Oswin, A.E. Haddrell, C. Hughes, M. Otero-Fernandez, R.J. Thomas, J.P. Reid, Oxidative stress contributes to bacterial airborne loss of viability, *Microbiol. Spectr.* 11 (2023) e03347-03322, <https://doi.org/10.1128/spectrum.03347-22>.

[22] S. Wang, Y. Zhao, A.W. Chan, M. Yao, Z. Chen, J.P. Abbatt, Organic peroxides in aerosol: key reactive intermediates for multiphase processes in the atmosphere, *Chem. Rev.* 123 (2023) 1635–1679, <https://doi.org/10.1021/acs.chemrev.2c00430>.

[23] R. Yang, G. Song, L. Wang, Z. Yang, J. Zhang, X. Zhang, S. Wang, L. Ding, N. Ren, A. Wang, X. Yu, Full solar-spectrum-driven antibacterial therapy over hierarchical $Sn_3O_4/PDINH$ with enhanced photocatalytic activity, *Small* 17 (2021) 2102744, <https://doi.org/10.1002/smll.202102744>.

[24] J. Tao, L. Zhang, K. Ho, R. Zhang, Z. Lin, Z. Zhang, M. Lin, J. Cao, S. Liu, G. Wang, Impact of $PM_{2.5}$ chemical compositions on aerosol light scattering in Guangzhou—the largest megalacity in South China, *Atmos. Res.* 135 (2014) 48–58, <https://doi.org/10.1016/j.atmosres.2013.08.015>.

[25] X. Xu, W. Zhao, X. Qian, S. Wang, B. Fang, Q. Zhang, W. Zhang, D.S. Venables, W. Chen, Y. Huang, The influence of photochemical aging on light absorption of atmospheric black carbon and aerosol single-scattering albedo, *Atmos. Chem. Phys.* 18 (2018) 16829–16844, <https://doi.org/10.5194/acp-18-16829-2018>.

[26] D. Vione, V. Maurino, C. Minero, E. Pelizzetti, M.A. Harrison, R.-I. Olariu, C. Arsene, Photochemical reactions in the tropospheric aqueous phase and on particulate matter, *Chem. Soc. Rev.* 35 (2006) 441–453, <https://doi.org/10.1039/b510796m>.

[27] Y. Wang, D.D. Huang, W. Huang, B. Liu, Q. Chen, R. Huang, M. Gen, B.R. G. Mabato, C.K. Chan, X. Li, Enhanced nitrite production from the aqueous photolysis of nitrate in the presence of vanillic acid and implications for the roles of light-absorbing organics, *Environ. Sci. Technol.* 55 (2021) 15694–15704, <https://doi.org/10.1021/acs.estlett.1c04642>.

[28] M. Gen, Z. Liang, R. Zhang, B.R.G. Mabato, C.K. Chan, Particulate nitrate photolysis in the atmosphere, *Environ. Sci.: Atmos.* 2 (2022) 111–127, <https://doi.org/10.1039/D1EA00087J>.

[29] M. Gen, R. Zhang, D.D. Huang, Y. Li, C.K. Chan, Heterogeneous SO_2 oxidation in sulfate formation by photolysis of particulate nitrate, *Environ. Sci. Technol. Lett.* 6 (2019) 86–91, <https://doi.org/10.1021/acs.estlett.8b00681>.

[30] F. Lian, Y. Zhang, S. Gu, Y. Han, X. Cao, Z. Wang, B. Xing, Photochemical transformation and catalytic activity of dissolved black nitrogen released from environmental black carbon, *Environ. Sci. Technol.* 55 (2021) 6476–6484, <https://doi.org/10.1021/acs.est.1c00392>.

[31] J. Liu, G. Dong, J. Jing, S. Zhang, Y. Huang, W. Ho, Photocatalytic reactive oxygen species generation activity of TiO_2 improved by the modification of persistent free radicals, *Environ. Sci. Nano* 8 (2021) 3846–3854, <https://doi.org/10.1039/D1EN00832C>.

[32] X. Hu, Z. Guo, W. Sun, X. Lian, Y. Fu, H. Meng, Y. Zhu, G. Zhang, X. Wang, L. Xue, Atmospheric processing of particulate imidazole compounds driven by photochemistry, *Environ. Sci. Nano* 9 (2022) 265–271, <https://doi.org/10.1021/acs.estlett.2c00029>.

[33] Z. Mu, Q. Chen, L. Zhang, D. Guan, H. Li, Photodegradation of atmospheric chromophores: Changes in oxidation state and photochemical reactivity, *Atmos. Chem. Phys.* 21 (2021) 11581–11591, <https://doi.org/10.5194/acp-21-11581-2021>.

[34] W. Nie, C. Yan, D.D. Huang, Z. Wang, Y. Liu, X. Qiao, Y. Guo, L. Tian, P. Zheng, Z. Xu, Secondary organic aerosol formed by condensing anthropogenic vapours over China's megalities, *Nat. Geosci.* 15 (2022) 255–261, <https://doi.org/10.1038/s41561-022-00922-5>.

[35] Q. Ge, Y. Liu, K. Li, L. Xie, X. Ruan, W. Wang, L. Wang, T. Wang, W. You, L. Zhang, Significant acceleration of photocatalytic CO_2 reduction at the gas-liquid interface of microdroplets, *Angew. Chem. Int. Ed.* (2023) e202304189, <https://doi.org/10.1002/anie.202304189>.

[36] T. Gerbich, H.-C. Schmitt, I. Fischer, J. Petersen, J. Albert, R. Mitric, Time-resolved study of 1, 8-naphthalic anhydride and 1, 4, 5, 8-naphthalene-tetracarboxylic dianhydride, *J. Phys. Chem. A* 119 (2015) 6006–6016, <https://doi.org/10.1021/jp511843q>.

[37] S. Sánchez, A.Y.Y. Woo, T. Baumgartner, Electron-accepting π -conjugated species with 1, 8-naphthalic anhydride or diketophosphanyl units, *Mater. Chem. Front.* 1 (2017) 2324–2334, <https://doi.org/10.1039/C7QM00336F>.

[38] L. Wang, Y. Shi, Y. Zhao, H. Liu, X. Li, M. Bai, Push-pull¹ 1, 8-naphthalic anhydride with multiple triphenylamine groups as electron donor, *J. Mol. Struct.* 1056–1057 (2014) 339–346, <https://doi.org/10.1016/j.molstruc.2013.10.004>.

[39] H. Li, S. Su, C. Liang, T. Zhang, X. An, M. Huang, H. Tao, X. Ma, Z. Ni, H. Tian, X. Chen, UV rewritable hybrid graphene/phosphor p–n junction photodiode, *ACS Appl. Mater. Interfaces* 11 (2019) 43351–43358, <https://doi.org/10.1021/acsami.9b14461>.

[40] B. Shi, Y. Li, F. Gao, J. Li, X. Cai, C. Zhang, Y. Wu, C. Lu, J. Wang, S. Liu, Enhancing the performance of perovskite solar cells by 4-chloro-1, 8-naphthalic anhydride for surface passivation, *Adv. Mater. Interfaces* 10 (2022) 2201809, <https://doi.org/10.1002/admi.202201809>.

[41] W. Zeng, H.-Y. Lai, W.-K. Lee, M. Jiao, Y.-J. Shiu, C. Zhong, S. Gong, T. Zhou, G. Xie, M. Sarma, K.-T. Wong, C.-C. Wu, C. Yang, Achieving nearly 30% external quantum efficiency for orange-red organic light emitting diodes by employing thermally activated delayed fluorescence emitters composed of 1, 8-naphthalimide-acridine hybrids, *Adv. Mater.* 30 (2018) 1704961, <https://doi.org/10.1002/adma.201704961>.

[42] Y. Tian, X. Li, D. Yin, Development of 4-oxime-1, 8-naphthalimide as a bioorthogonal turn-on probe for fluorogenic protein labeling, *Chem. Commun.* 55 (2019) 12865–12868, <https://doi.org/10.1039/C9CC06769H>.

[43] G. Noirbent, F. Dumur, Recent advances on naphthalic anhydrides and 1, 8-naphthalimide-based photoinitiators of polymerization, *Eur. Polym. J.* 132 (2020) 109702, <https://doi.org/10.1016/j.eurpolymj.2020.109702>.

[44] Z. Li, L. Zhang, Y. Liu, C. Shao, Y. Gao, F. Fan, J. Wang, J. Li, J. Yan, R. Li, Surface-polarity-induced spatial charge separation boosts photocatalytic overall water splitting on GaN nanorod arrays, *Angew. Chem. Int. Ed.* 59 (2020) 935–942, <https://doi.org/10.1002/anie.201912844>.

[45] Y. Guo, Q. Zhou, J. Nan, W. Shi, F. Cui, Y. Zhu, Perylenetetracarboxylic acid nanosheets with internal electric fields and anisotropic charge migration for photocatalytic hydrogen evolution, *Nat. Commun.* 13 (2022) 2067, <https://doi.org/10.1038/s41467-022-29826-z>.

[46] B. Yan, C. Du, G. Yang, Constructing built-in electric field in ultrathin graphitic carbon nitride nanosheets by N and O codoping for enhanced photocatalytic hydrogen evolution activity, *Small* 16 (2020) 1905700, <https://doi.org/10.1002/smll.201905700>.

[47] S. Gao, Q. Zhang, X. Su, X. Wu, X.-G. Zhang, Y. Guo, Z. Li, J. Wei, H. Wang, S. Zhang, J. Wang, Ingenious artificial leaf based on covalent organic framework membranes for boosting CO_2 photoreduction, *J. Am. Chem. Soc.* 145 (2023) 9520–9529, <https://doi.org/10.1021/jacs.2c11146>.

[48] R. Tang, H. Zeng, C. Feng, S. Xiong, L. Li, Z. Zhou, D. Gong, L. Tang, Y. Deng, Twisty C-TiO₂/PCN S-scheme heterojunction with enhanced $n\rightarrow\pi^*$ electronic excitation for promoted piezo-photocatalytic effect, *Small* (2023) 2207636, <https://doi.org/10.1002/smll.202207636>.

[49] Y. Guo, W. Shi, Y. Zhu, Enhanced photoactivity and oxidizing ability simultaneously via internal electric field and valence band position by crystal structure of bismuth oxyiodide, *Appl. Catal. B Environ.* 262 (2020) 118262, <https://doi.org/10.1016/j.apcatb.2019.118262>.

[50] Z. Qi, J. Chen, Q. Li, N. Wang, S.A. Carabineiro, K. Lv, Increasing the photocatalytic hydrogen generation activity of cds nanorods by introducing interfacial and polarization electric fields, *Small* (2023) 2303318, <https://doi.org/10.1002/smll.202303318>.

[51] D. Bury, M. Jakubczak, M.A.K. Purbayanto, A. Wojciechowska, D. Moszczyńska, A. M. Jastrzębska, Photocatalytic activity of the oxidation stabilized Ti_3C_2Tx MXene in decomposing methylene blue, bromocresol green and commercial textile dye, *Small Methods* (2023) 2201252, <https://doi.org/10.1002/smtd.202201252>.

[52] Y. Guo, W. Shi, Y. Zhu, Internal electric field engineering for steering photogenerated charge separation and enhancing photoactivity, *EcoMat* 1 (2019) e12007, <https://doi.org/10.1002/eom2.12007>.

[53] I. Grabtchev, T. Konstantinov, S. Guittouneau, P. Meallier, Photochemistry of some 1, 8-naphthalic anhydride derivatives, *Dyes Pigm* 35 (1997) 361–366, [https://doi.org/10.1016/S0143-7208\(96\)00116-7](https://doi.org/10.1016/S0143-7208(96)00116-7).

[54] W. He, H.-K. Kim, W.G. Wamer, D. Melka, J.H. Callahan, J.-J. Yin, Photogenerated charge carriers and reactive oxygen species in ZnO/Au hybrid nanostructures with enhanced photocatalytic and antibacterial activity, *J. Am. Chem. Soc.* 136 (2014) 750–757, <https://doi.org/10.1021/ja410800y>.

[55] X. Xu, R. Sa, W. Huang, Y. Sui, W. Chen, G. Zhou, X. Li, Y. Li, H. Zhong, Conjugated organic polymers with anthraquinone redox centers for efficient photocatalytic hydrogen peroxide production from water and oxygen under visible light irradiation without any additives, *ACS Catal.* 12 (2022) 12954–12963, <https://doi.org/10.1021/acscatal.2c04085>.

[56] X. Xu, H. Zhong, W. Huang, Y. Sui, R. Sa, W. Chen, G. Zhou, X. Li, D. Li, M. Wen, B. Jiang, The construction of conjugated organic polymers containing phenanthrenequinone redox centers for visible-light-driven H_2O_2 production from H_2O and O_2 without any additives, *Chem. Eng. J.* 454 (2023), <https://doi.org/10.1016/j.cej.2022.139929>.

[57] D. Liu, J. Wang, X. Bai, R. Zong, Y. Zhu, Self-assembled PDINH supramolecular system for photocatalysis under visible light, *Adv. Mater.* 28 (2016) 7284–7290, <https://doi.org/10.1002/adma.201601168>.

[58] Y. Li, Z. Jiang, G. Dong, W. Ho, Construction and activity of an all-organic heterojunction photocatalyst based on melem and pyromellitic dianhydride, *ChemSusChem* 15 (2022) e202200477, <https://doi.org/10.1002/cssc.202200477>.

[59] Z. Jiang, G. Dong, R. Wang, C. He, C. Wang, J. Sun, Enhanced interface charge transfer of Z-scheme photocatalyst by br substitution at the bay position in perylene tetracarboxylic diimide, *Sol. RRL* 4 (2020) 2000303, <https://doi.org/10.1002/solr.202000303>.

[60] J. Xu, Q. Gao, Z. Wang, Y. Zhu, An all-organic OD/2D supramolecular porphyrin/g-C₃N₄ heterojunction assembled via $\pi\cdot\pi$ interaction for efficient visible photocatalytic oxidation, *Appl. Catal. B: Environ.* 291 (2021) 120059, <https://doi.org/10.1016/j.apcatb.2021.120059>.

[61] Q. Li, Y. Jiao, Y. Tang, J. Zhou, B. Wu, B. Jiang, H. Fu, Shear stress triggers ultrathin-nanosheet carbon nitride assembly for photocatalytic H_2O_2 production coupled with selective alcohol oxidation, *J. Am. Chem. Soc.* 145 (2023) 20837–20848, <https://doi.org/10.1021/jacs.3c05234>.

[62] H. Ben, G. Yan, H. Liu, C. Ling, Y. Fan, X. Zhang, Local spatial polarization induced efficient charge separation of squaraine-linked COF for enhanced photocatalytic performance, *Adv. Funct. Mater.* 32 (2022) 2104519, <https://doi.org/10.1002/adfm.202104519>.

[63] X. Zhang, L. Du, W. Zhao, Z. Zhao, Y. Xiong, X. He, P.F. Gao, P. Alam, C. Wang, Z. Li, Ultralong UV/mechanical-excited room temperature phosphorescence from purely organic cluster excitons, *Nat. Commun.* 10 (2019) 5161, <https://doi.org/10.1038/s41467-019-13048-x>.

[64] D. Liu, X. Yang, P. Chen, X. Zhang, G. Chen, Q. Guo, H. Hou, Y. Li, Rational design of PDI-based linear conjugated polymers for highly effective and long-term

photocatalytic oxygen evolution, *Adv. Mater.* (2023) 2300655, <https://doi.org/10.1002/adma.202300655>.

[65] G. Wan, L. Yin, X. Chen, X. Xu, J. Huang, C. Zhen, H. Zhu, B. Huang, W. Hu, Z. Ren, H. Tian, L. Wang, G. Liu, H.-M. Cheng, Photocatalytic overall water splitting over PbTiO₃ modulated by oxygen vacancy and ferroelectric polarization, *J. Am. Chem. Soc.* 144 (2022) 20342–20350, <https://doi.org/10.1021/jacs.2c08177>.

[66] J. Luo, Y. Liu, C. Fan, L. Tang, S. Yang, M. Liu, M. Wang, C. Feng, X. Ouyang, L. Wang, L. Xu, J. Wang, M. Yan, Direct attack and indirect transfer mechanisms dominated by reactive oxygen species for photocatalytic H₂O₂ production on g-C₃N₄ possessing nitrogen vacancies, *ACS Catal.* 11 (2021) 11440–11450, <https://doi.org/10.1021/acscatal.1c03103>.

[67] Q. Zhang, L. Li, Q. Zhou, H. Zhang, H. Zhang, B. An, H. Ning, T. Xing, M. Wang, M. Wu, W. Wu, Boosting C₃H₆ epoxidation via tandem photocatalytic H₂O₂ production over nitrogen-vacancy carbon nitride, *ACS Catal.* 13 (2023) 13101–13110, <https://doi.org/10.1021/acscatal.3c02904>.

[68] P.D.M. Phan, D.-V. Nguyen, N.H. Anh, H.P. Toan, P.P. Ly, D.-P. Bui, S.H. Hur, T.D. T. Ung, D.D. Bich, H.-T. Vuong, S-Scheme Heterostructured CdS/g-C₃N₄ Nanocatalysts for Piezo-Photocatalytic Synthesis of H₂O₂, *ACS Appl. Nano Mater.* 6 (2023) 16702–16715, <https://doi.org/10.1021/acsnano.3c02933>.

[69] J. Luo, C. Feng, C. Fan, L. Tang, Y. Liu, Z. Gong, T. Wu, X. Zhen, H. Feng, M. Yan, L. Wang, L. Xu, Enhanced indirect attack behavior of ¹O₂ for photocatalytic H₂O₂ production: Possible synergistic regulation of spin polarization and water bridge on photocatalytic reaction, *J. Catal.* 413 (2022) 1132–1145, <https://doi.org/10.1016/j.jcat.2022.08.019>.

[70] J. Sun, W. Peng, B. Fan, D. Gan, L. Li, P. Liu, J. Shen, Tertiary amines convert 1O₂ to H₂O₂ with enhanced photodynamic antibacterial efficiency, *J. Hazard. Mater.* 435 (2022) 128948, <https://doi.org/10.1016/j.jhazmat.2022.128948>.

[71] J. Cheng, S. Wan, S. Cao, Promoting solar-driven hydrogen peroxide production over thiazole-based conjugated polymers via generating and converting singlet oxygen, *Angew. Chem. Int. Ed.* 62 (2023) e202310476, <https://doi.org/10.1002/anie.202310476>.